

Surface-directed spinodal decomposition in a stressed, two-dimensional, thin film

S.M. Wise^{a,*}, J.S. Kim^a, W.C. Johnson^b

^aMathematics Department, University of California, 103 MSTB, Irvine, CA 926973875, USA

^bDepartment of Materials Science and Engineering, University of Virginia; Charlottesville, VA, USA

Received 18 November 2003; received in revised form 12 May 2004; accepted 22 July 2004

Available online 11 September 2004

Abstract

Two-dimensional simulations of the spinodal decomposition of self-stressed, binary thin films using a Cahn–Hilliard model are presented. Two different sets of mechanical boundary conditions are considered, and compositional strains for a cubic–anisotropic system under plane strain are treated. A composition-dependent interaction energy is assumed at the free surface. Numerical solution of the coupled Cahn–Hilliard and elastic equilibrium equations are obtained using an efficient nonlinear multigrid method. Results of simulations show that, for large enough compositional strain, surface-directed decomposition occurs at the traction-free surface, even when there is negligible surface interaction energy initially attracting one of the components. This decomposition is controlled by elasticity, and results in a local alignment of phases perpendicular to the free surface, in contrast to the parallel alignment produced by surface energy in stress-free systems.

© 2004 Elsevier B.V. All rights reserved.

PACS: 64.70.Kb

Keywords: Computer simulation; Phase transitions; Surface stress; Wetting

1. Introduction

The process of spinodal decomposition in a bulk, binary alloy is well understood [1,2]. When an initially homogeneous mixture is rapidly quenched into a region of thermodynamic instability in the temperature–composition plane, phase decomposition occurs by long-range diffusion. The process is one of nucleation and growth, when the mixture is quenched to inside the metastable region of the phase diagram. When the mixture is quenched to inside the spinodal region, however, the alloy is unstable with respect to infinitesimal composition fluctuations above a certain wavelength and decomposition proceeds without a nucleation barrier. In bulk alloys for which interfacial and elastic energies can be neglected, the composition fluctuations grow, resulting in a random, isotropic microstructure, comprised of separated *A*- and *B*-rich phase regions.

The kinetics of spinodal decomposition and the resulting microstructure can be significantly modified in the presence of an interface or free surface [3–8]. One simple way to account for the effect of a surface on decomposition is to introduce a composition-dependent, short-range interaction between the mixture and the surface into the free energy functional for the system energy [9,3,5,7]. (Surface biasing effects have also been modelled as due to large surface temperature gradients [3] and long-range interaction energies [4].) One prediction of such models is a preferential segregation of one component over the other to the surface in the initial stages of decomposition. This segregation sets up a fluctuation in the composition field, perpendicular to the free surface, which grows so as to form alternating *A*-rich and *B*-rich layers parallel to the surface. If the chemical interaction of a component with the surface is sufficiently strong, the evolved microstructure can become aligned with the geometry of the surface, even far into the interior regions. This phenomenon is known as *surface-directed* spinodal decomposition, and has been observed

* Corresponding author. Tel.: +1 949 824 6439; fax: +1 949 824 7993.
E-mail address: swise@math.uci.edu (S.M. Wise).

experimentally in polymer films [10–12] and solid-state decomposition [13].

From Cahn's seminal treatment of spinodal decomposition [2], it has been clear that coherency stresses arising from a variety of sources, including compositional strains and an applied stress, strongly influence the development of microstructure. More recent work has demonstrated that coherency stresses, like the surface interaction energy, can also have a strong effect on the characteristics of near-surface decomposition [14–16]. Cahn and Kobayashi [14] investigated the competing effects of surface interaction and stress on spinodal decomposition in one-dimensional, bending thin plates. More recently, Seol et al. [15,16] explored the three-dimensional spinodal decomposition of a self-stressed, binary alloy near a traction-free surface. In particular, in Refs. [15,16] it was shown that spinodal decomposition may be surface-directed, even without a surface interaction energy. Such an effect, which was noted in Ref. [17] for two-dimensional thin films, results because the coherency strains that accompany phase separation are relaxed much more readily at the free surface than in the interior of the crystal.

The purpose of this work is to explore the combined effects of self-stress and surface interaction on spinodal decomposition in initially homogeneous, two-dimensional thin films. The model presented here differs in several ways from the one employed by [15,16]: (i) we use a degenerate mobility and a logarithmic regular solution model, which pose significant numerical challenges, (ii) we include a surface interaction energy in the free energy functional, and (iii) we solve directly the Cauchy–Navier equations for elasticity. On the last point, by contrast, Seol et al. [15,16] solve the elasticity problem using Khachatryan's approximation method [18], albeit in three dimensions.

In Section 2, we present a two-dimensional, Cahn–Hilliard model which describes spinodal decomposition in a binary, cubic, thin-film system with two parallel surfaces. Stresses arise from the compositional dependence of the lattice parameter and there is a short-range chemical interaction at the surfaces. Two sets of mechanical boundary conditions are considered, edge-supported and bottom-supported. The results of the numerical simulations are reported and discussed in Section 3. In Section 4 we summarize the investigation. Finally, in Appendix A we describe briefly the nonlinear multigrid method that is used to solve the system of equations.

2. Governing equations

In this section, we present the governing equations and boundary conditions used to simulate the spinodal decomposition of two self-stressed, binary, thin-film systems. Governing equations are presented in dimensionless form. Briefly, we employ a characteristic length, $\mathcal{L} = (\kappa_v/\rho_o kT)^{1/2}$, where κ_v is the Cahn–Hilliard gradient energy coefficient, ρ_o is the density of lattice sites, k is

Boltzmann's constant, and T is the absolute temperature. The characteristic time is defined as $\mathcal{T} = \mathcal{L}^2/M\rho_o kT$, where M is the mobility of atoms in the phase decomposing film. Energy densities, the stress tensor, and the elastic constants are scaled by ρ_o . Further details of the non-dimensionalization are available in Ref. [17].

2.1. Free energy

We begin by formulating the free energy for an isothermal, two-dimensional, binary material, occupying the general region D , and bounded by the curve B . The (possibly disconnected) curve B_1 is that portion of B on which an external traction \vec{t} is specified. On the remaining portion of the boundary the material is clamped; i.e., the displacement on the surface is specified. Plane strain conditions are assumed in calculating the elastic fields for the two-dimensional structure and the [010] crystal axis of the cubic film is perpendicular to the surface plane as shown in Fig. 1.

We express the total dimensionless free energy of the system, \mathcal{F} , as a functional of the form [1]

$$\mathcal{F} = \int_D \left\{ f_{ch}(c) + f_{el}(u_i, \partial_{x_j} u_i, c) + \frac{1}{2} |\nabla c|^2 \right\} d^2 \vec{x} + \oint_B f_s(c) d\ell - \int_{B_1} \vec{t} \vec{u} d\ell, \quad (1)$$

where c is the composition and \vec{u} is the vector of material displacements. f_{ch} is the chemical energy density of a stress-free homogeneous system of the indicated composition, f_{el} is the elastic energy density, and $1/2 |\nabla c|^2$ is the gradient energy density. f_s gives the interaction energy density between the film and surface and is assumed to be a function of the film composition at the surface. The second surface integral gives the mechanical work done by the external traction, \vec{t} , acting on B_1 . Taking the material to be isolated, the following mass constraint is added:

$$\int_D (c(\vec{x}, t) - c_o) d^2 \vec{x} = 0, \quad (2)$$

where c_o is the average value of c in D .

The chemical energy density, f_{ch} , follows a regular solution model:

$$f_{ch}(c) = c \ln(c) + (1-c) \ln(1-c) + 2c(1-c)/\theta, \quad (3)$$

where θ is the scaled temperature. If $\theta < 1$, the chemical energy density displays a miscibility gap.

In full, three-dimensional form, the elastic energy density is given by

$$f_{el} = \sum_{i,j=1}^3 T_{ij} [E_{ij} - e(c) \delta_{ij}] / 2. \quad (4)$$

T_{ij} and $E_{ij} = (\partial_{x_j} u_i + \partial_{x_i} u_j) / 2$ are the Cauchy stress and linearized strain tensors, respectively; e is the eigenstrain and is here taken to follow Vegard's law: $e(c) = \eta(c - c_o)$, where η is a dimensionless parameter which gives the

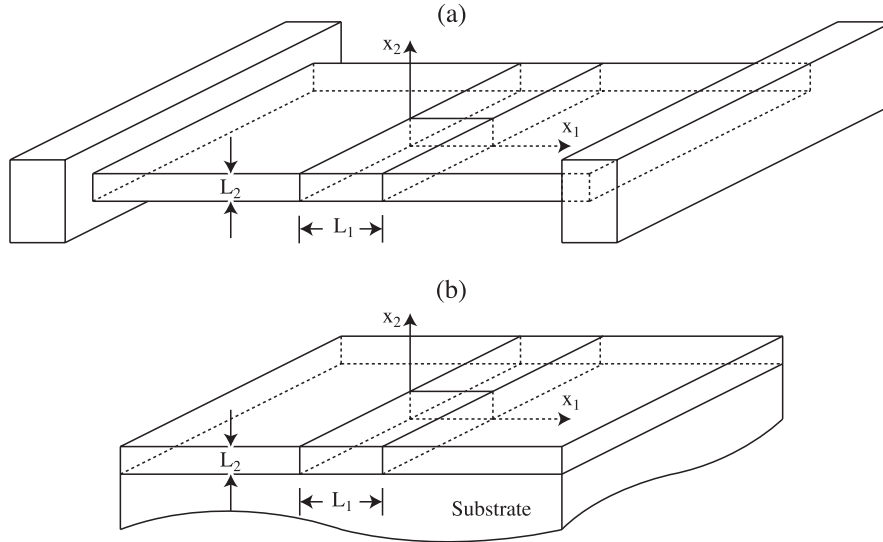


Fig. 1. Schematic illustrations of the (a) edge-supported and (b) bottom-supported thin-film systems. The systems are two-dimensional, i.e., $c=c(x_1, x_2)$, and plane-strain conditions are assumed.

composition dependence of the lattice parameter. The stress and strain tensors are related by

$$T_{ij} = \sum_{k,l=1}^3 C_{ijkl} [E_{kl} - e(c)\delta_{kl}], \quad i, j = 1, 2, 3, \quad (5)$$

where C_{ijkl} is the elastic stiffness tensor. We assume that the material is cubic–anisotropic and homogeneous, for which

$$C_{ijkl} = C_{12}\delta_{ij}\delta_{kl} + C_{44}(\delta_{ik}\delta_{jl} + \delta_{il}\delta_{jk}) + (C_{11} - C_{12} - 2C_{44})\delta_{ijkl}, \quad (6)$$

with $\delta_{ijkl}=1$ only if $i=j=k=l$ and $\delta_{ijkl}=0$ otherwise. C_{11} , C_{12} and C_{44} are the cubic elastic constants. As mentioned, the conditions for plain strain, which are expressed mathematically by $u_1=u_1(x_1, x_2)$, $u_2=u_2(x_1, x_2)$, and $u_3=0$, are assumed. It then follows that E_{13} , E_{23} and E_{33} all vanish in the thin film.

We assume f_s to act over a very short range, to be independent of the state of deformation, and to depend linearly on composition. A suitable form for f_s is [9]

$$f_s(c) = s_0 + s_1c, \quad (7)$$

where s_0 and s_1 are constants. This first-order relation is compatible with nearest-neighbor bond-counting approximations. We will assume that f_s acts only on B_1 , the boundary on which the traction is specified.

2.2. Dynamical equations

The evolution of the composition field in the film is determined by the mass conservation equation,

$$\frac{\partial c}{\partial t} = -\nabla \cdot \vec{J}, \quad (8)$$

where $\vec{J} = (J_1, J_2)^T$ is the compositional flux. We assume that the flux is given as

$$\vec{J} = -c(1-c)\nabla\mu, \quad (9)$$

where $c(1-c)$ is the degenerate mobility and μ is a generalized chemical potential, defined as

$$\mu = \frac{\delta\mathcal{F}}{\delta c} = \frac{df_{ch}}{dc} + \frac{\partial f_{el}}{\partial c} - \nabla^2 c. \quad (10)$$

The result is the Cahn–Hilliard (CH) equation

$$\frac{\partial c}{\partial t} = \nabla \cdot \left[c(1-c)\nabla \left(\frac{df_{ch}}{dc} + \frac{\partial f_{el}}{\partial c} - \nabla^2 c \right) \right]. \quad (11)$$

Since in crystalline materials elastic relaxation occurs on a much faster time scale than that of diffusion, we may assume that elastic equilibrium always obtains. Thus the quasi-steady Cauchy–Navier equations hold for all time:

$$\frac{\partial^2 u_2}{\partial x_1 \partial x_2} + \alpha_1 \frac{\partial^2 u_1}{\partial x_1^2} + \alpha_2 \frac{\partial^2 u_1}{\partial x_2^2} = \alpha_3 \frac{\partial e}{\partial x_1}, \quad (12)$$

$$\frac{\partial^2 u_1}{\partial x_1 \partial x_2} + \alpha_2 \frac{\partial^2 u_2}{\partial x_1^2} + \alpha_1 \frac{\partial^2 u_2}{\partial x_2^2} = \alpha_3 \frac{\partial e}{\partial x_2}, \quad (13)$$

where

$$\alpha_1 = \frac{C_{11}}{C_{44} + C_{12}}, \quad \alpha_2 = \frac{C_{44}}{C_{44} + C_{12}} \quad \text{and} \quad \alpha_3 = \frac{2C_{12} + C_{11}}{C_{44} + C_{12}}. \quad (14)$$

2.3. Boundary conditions

Two types of thin-film systems are considered in this work. The first is the edge-supported thin film, Fig. 1a, and the second is the bottom-supported thin film, Fig. 1b. The

supports (substrate) to which the films are bonded are considered rigid and inert with respect to mass exchange and chemical interaction with the film. The air-film interfaces are assumed free of external tractions, i.e., $\vec{\tau} = \vec{0}$, on B_1 . Calculations are restricted to the two-dimensional computational cell, a subregion of D defined by $0 \leq x_1 \leq L_1$ and $0 \leq x_2 \leq L_2$, referring to the coordinate systems in Fig. 1.

The boundary conditions for the edge-supported film assume mechanical and thermodynamic equilibrium at all surfaces. They are summarized as

$$T_{12}(x_1, 0) = T_{22}(x_1, 0) = 0,$$

$$T_{12}(x_1, L_2) = T_{22}(x_1, L_2) = 0,$$

$$\vec{u}(0, x_2) = \vec{u}(L_1, x_2), \quad \partial_{x_1} \vec{u}(0, x_2) = \partial_{x_1} \vec{u}(L_1, x_2),$$

$$\partial_{x_2} c(x_1, 0) = s_1, \quad \partial_{x_2} c(x_1, L_2) = -s_1,$$

$$c(0, x_2) = c(L_1, x_2), \quad \partial_{x_1} c(0, x_2) = \partial_{x_1} c(L_1, x_2),$$

$$J_2(x_1, 0) = J_2(x_1, L_2) = 0,$$

$$J_1(0, x_2) = J_1(L_1, x_2), \quad \partial_{x_1} J_1(0, x_2) = \partial_{x_1} J_1(L_1, x_2) \quad (15)$$

The flux conditions are chosen so that there is no mass flow perpendicular to the free surfaces. The composition field is assumed periodic in the x_1 direction. The boundary conditions for the bottom-supported film are the same as those for the edge-supported film except that the conditions at $x_2=0$ are replaced by $\vec{u}(x_1, 0) = \vec{0}$, $\partial_{x_2} c(x_1, 0)=0$, and $J_2(x_1, 0)=0$.

3. Simulation results

3.1. Parameters

The chemical energy density of the film is defined using the scaled temperature $\theta=0.8$. As this is below the critical temperature $\theta_c=1$, the chemical energy, plotted in Fig. 2, displays a miscibility gap. The stress-free phase equilibria and chemical spinodal boundaries of the film are given by $c_{\text{eq}}^- = 0.1448$, $c_{\text{eq}}^+ = 0.8552$ and $c_{\text{sp}}^- = 0.2764$, $c_{\text{sp}}^+ = 0.7236$, respectively. In the simulations the average composition of the film is taken to be either the critical composition $c_o = 0.5$ or $c_o = 0.4$, both of which are inside the chemical spinodal. Initially, the composition field is nearly homogeneous, with random fluctuations of maximum magnitude 10^{-4} about the average film composition.

We consider surface free energy coefficients with magnitudes $|s_1|=0.0, 0.001, 0.01$ or 0.1 . The sign of s_1 determines whether A or B atoms are energetically preferred at the surface; if positive, A atoms are preferred, if negative

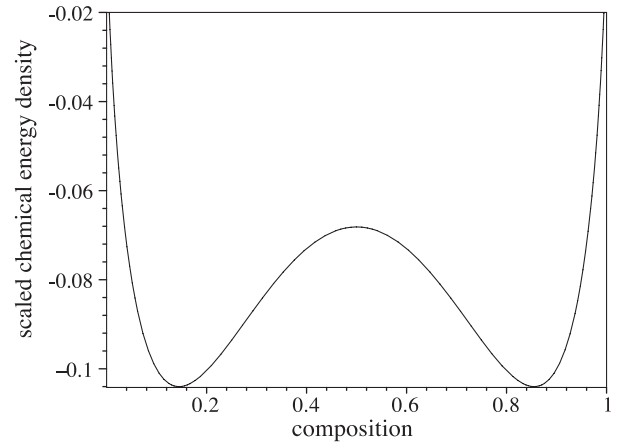


Fig. 2. The chemical energy density of the film, $f_{\text{ch}}(c)$, is plotted as a function of composition at scaled temperature $\theta=0.8$. The stress-free phase equilibria and chemical spinodal boundaries of the film are given by $c_{\text{eq}}^- = 0.1448$, $c_{\text{eq}}^+ = 0.8552$ and $c_{\text{sp}}^- = 0.2764$, $c_{\text{sp}}^+ = 0.7236$, respectively.

B atoms are preferred. The scaled cubic elastic constants are $C_{11}=500$, $C_{12}=190$ and $C_{44}=240$, chosen to correspond to the elastic anisotropy of silicon. Compositional strains, η , of 1, 2, and 3% are considered.

The width of the computational cell is taken as $L_1=90$; the height is taken as either $L_2=45$ or 90 . Simulations are performed using the spatial step size $h=45/64$ and the temporal step size $s=0.05$.

3.2. Discussion

Figs. 3–15 display gray-scale contour plots of the composition field at the indicated non-dimensional times. The A -rich and B -rich phases are represented by black and white, respectively; compositions lying between those which define the A -rich and B -rich phases are represented on the gray scale. Figs. 3–9 display simulation results for edge-supported thin films; Figs. 10–15 display simulation results for bottom-supported thin films.

3.2.1. Edge-supported thin films

Fig. 3 depicts the microstructural evolution of two, stress-free ($\eta=0$), edge-supported thin films. Both have an average composition of $c_o=0.5$, and non-dimensional thickness of $L_2=45$. In Fig. 3a the surface energy parameter is $s_1=0.001$, and in Fig. 3b $s_1=0.01$. In both cases the surface energy is lowered by the presence of A -rich phase at the surface.

In the initial stages of decomposition, A atoms segregate to the free surfaces at the top and bottom of the cells ($t=60$). This segregation sets up a fluctuation in the composition perpendicular to the free surface, which grows, forming alternating A -rich (black) and B -rich (white) layers parallel to the surface ($t=120$). In Fig. 3b, the interaction term is sufficiently large that the entire microstructure becomes aligned horizontally. The surface interaction term used in Fig. 3a is weaker than that used in Fig. 3b, and it does not

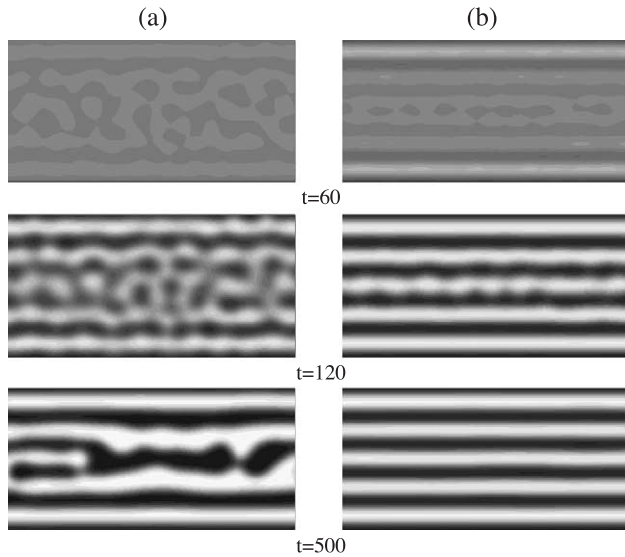


Fig. 3. The microstructural evolutions of two stress-free, edge-supported films of composition $c_o=0.5$ are depicted up to scaled time $t=500$. ($L_2=45$ and $\eta=0$). The surface interaction parameters are (a) $s_1=0.001$ and (b) $s_1=0.01$. Alignment of the phases parallel to the surface occurs in both cases due to the interaction of the film and surface. In (a), the kinetics of the surface-directed decomposition are not fast enough for the layered structure to spread through the film before random fluctuations in the interior of the film have a chance to grow.

lead to sufficiently rapid kinetics perpendicular to the surface to overcome the growth of random fluctuations in the interior of the film. In this case, only a partial horizontal alignment of the phases emerges. As the magnitude of the surface interaction term is further reduced, progressively less alignment is observed.

This type of decomposition, known as *surface-directed spinodal decomposition*, has been modelled previously [3–7]. The characteristic feature of surface-directed spinodal decomposition in stress-free systems is the formation of alternating *A*- and *B*-rich layers parallel to the planar surface. With the addition of elasticity to the dynamical model, this feature can be qualitatively modified, as shown in the following figures.

Fig. 4 depicts the microstructural evolution of two stressed, edge-supported films of composition $c_o=0.5$. The non-dimensional film thickness is the same as in Fig. 3: $L_2=45$. Unlike Fig. 3, however, there is no chemical interaction between the film and the surface ($s_1=0$), and elastic fields arise owing to compositional inhomogeneity. In Fig. 4a $\eta=0.01$, and in Fig. 4b $\eta=0.02$.

The microstructural evolution depicted in Fig. 4a is not noticeably different from what is seen in the stress-free case ($\eta=0$): Random composition fluctuations grow forming an isotropic, interconnected microstructure. In Fig. 4b the situation is different. Decomposition occurs initially on the free surfaces, with the formation of regularly spaced, alternating *A*-rich (black) and *B*-rich (white) ($t=180$) regions. Lamellar structures then grow *perpendicular* to the top and bottom surfaces ($t=260$ and $t=340$), establishing

a vertical alignment of the microstructure. The two lamellar structures ultimately link up in the middle of the film ($t=500$).

This type of decomposition is dramatically different from the process depicted in Fig. 3. Both may be characterized as surface-directed spinodal decomposition, since decomposition is strongly influenced by the surface. However, whereas the phase alignment produced exclusively by a surface interaction energy was parallel to the free surface, the phase alignment produced by the compositional strains, at least in this instance, is perpendicular to the surface. To help understand why this alignment is elastically preferred, it is useful to analyze the role of elasticity in spinodal decomposition.

Consider a bulk, initially homogeneous mixture of critical composition, $c_o=0.5$, and suppose that the symmetric free energy density shown in Fig. 2 applies. At the initial state, if there are no composition fluctuations, the eigen-strain and the displacements both vanish. Hence, the elastic energy vanishes. If there are composition fluctuations, the chemical energy of the system is reduced by their growth.

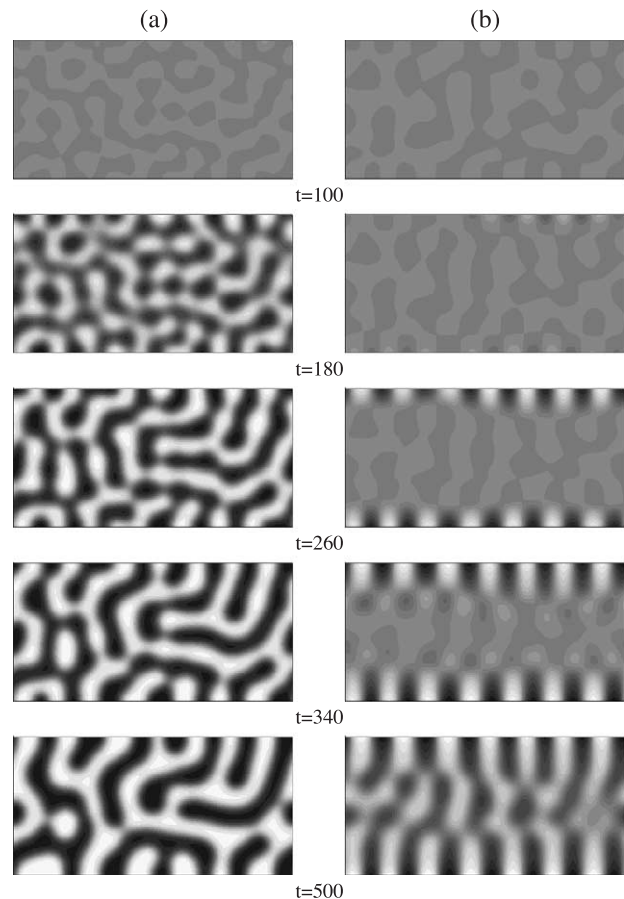


Fig. 4. The microstructural evolutions of two differently stressed, edge-supported films of composition $c_o=0.5$ are depicted for $L_2=45$ and $s_1=0$. The compositional strains are (a) $\eta=0.01$ and (b) $\eta=0.02$. There is no surface directed decomposition in (a). In (b), surface-directed spinodal decomposition occurs with the phases oriented *perpendicular* to the surface in order to relieve some of the compositional strains.

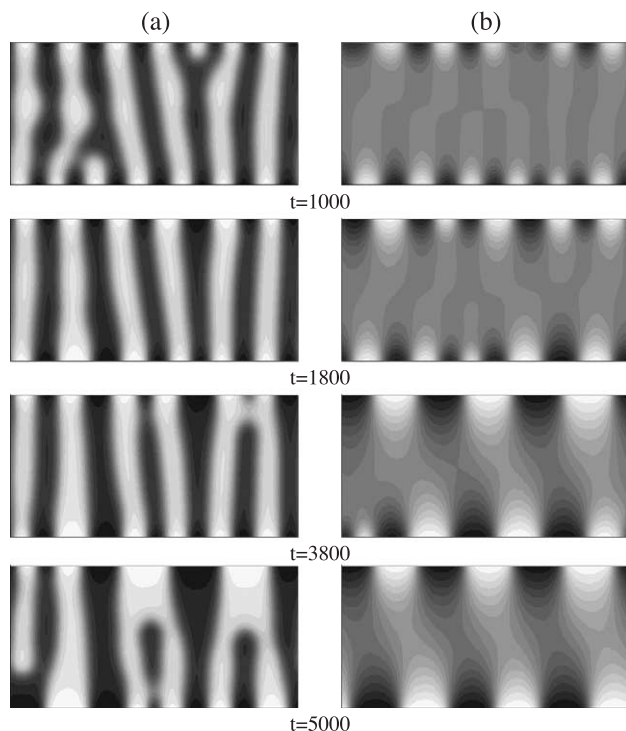


Fig. 5. The long-time evolutions of two self-stressed, edge-supported films of composition $c_0=0.5$ are depicted to $t=5000$. As in Fig. 4b, $L_2=45$ and $s_1=0$. In (a) ($\eta=0.02$) the further evolution of the film from Fig. 4b is shown. The system evolves to an arrangement of alternating, vertical layers of A -rich (black) and B -rich (white) phases. In (b) ($\eta=0.03$) the elastic energy partially suppresses separation in the interior of the film, yet the system still aligns vertically. Such arrangements of phases in (a) and (b) require no overall displacement in the horizontal direction.

But the fluctuations grow only if the driving force of the chemical energy can overcome the interfacial and elastic energies, both of which are minimized with a uniform mixture. In other words, the elasticity acts to suppress the growth of fluctuations, and succeeds if it is strong enough relative to sum of the other contributions [2].

Every point in space is essentially the same for a bulk system, as it pertains to the growth of a composition fluctuation. When a surface is present, however, the situation is different. The growth of a composition fluctuation in the vicinity of the traction-free surface would be expected to grow more readily than in the bulk (interior regions), because the compositional stresses are relaxed near a surface. For this reason, spinodal decomposition initiates at the unconstrained surfaces (top and bottom) in Fig. 4b.

The vertical alignment produced during the initial stages of decomposition is due to another aspect of the elasticity, namely the periodic displacement boundary conditions at the side edges of the film. Because of these conditions, no net expansion or contraction of the film occurs in the horizontal direction. (The same is true for clamped side boundary conditions.) Since the chemical free energy density (Fig. 2) is symmetric, the A -rich (black) and B -rich (white) phases have the same magnitude of eigenstrain ($e=\eta(c-c_0)$), but with different signs. Thus alternating

vertical layers of equal width give no net horizontal (x_1) displacement. In fact, this arrangement is elastically preferred over one with layers parallel to the surface. This explains the vertical alignment of the growing phases in Fig. 4b.

Fig. 5a shows the subsequent evolution, to $t=5000$, of the film in Fig. 4b. After much coarsening, the number of layers is reduced, which eliminates some interfacial energy. But the vertical alignment of the microstructure is maintained, suggesting that it is elastically preferred. Fig 5b depicts the long-time evolution of a film with eigenstrain $\eta=0.03$ (all other parameters are as in Figs. 4b and 5a). The elastic energy has a more pronounced effect on microstructural evolution in Fig. 5b than in 5a: It delays the onset of surface decomposition (with respect to (a)), it allows for very little random decomposition in the interior of the film, and it partially suppress phase separation in the interior of the film. As in Fig. 5a, the system undergoes a coarsening process

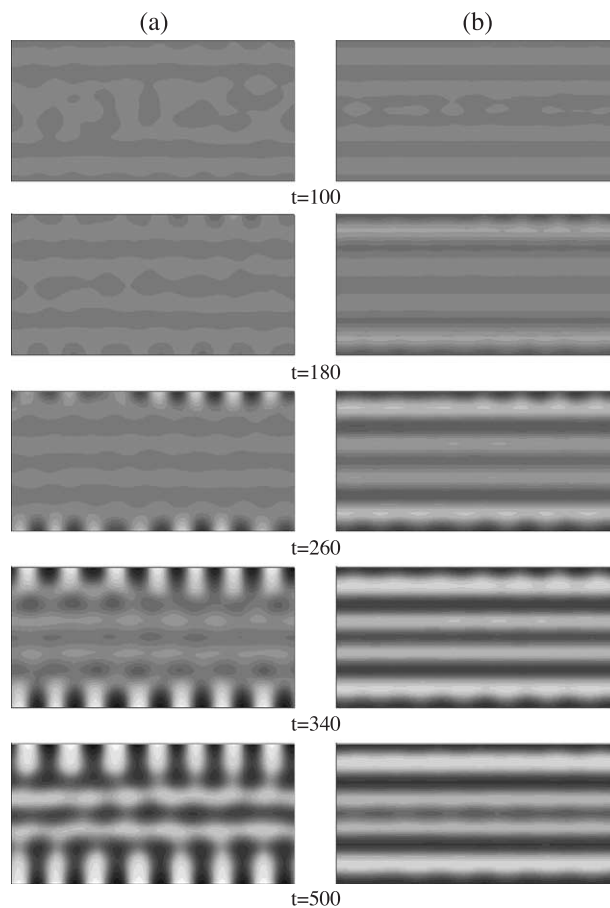


Fig. 6. The microstructural evolutions of two stressed, edge-supported films of composition $c_0=0.5$ are depicted to $t=500$ for film thickness $L_2=45$ and compositional strain $\eta=0.02$. In (a) ($s_1=0.001$), a thin A -rich (dark gray) surface layer forms in the early stages of decomposition, due to the surface interaction. The elastic energy destabilizes this layer leading to a vertical realign of the microstructure. In (b) ($s_1=0.01$), the surface interaction is stronger and the kinetics are sufficiently fast to allow a horizontal alignment through the thickness of the film. At longer times, the strain destabilizes the horizontal layers and a vertical alignment of the phases develops. (The evolution at long times resembles that appearing in Fig. 11).

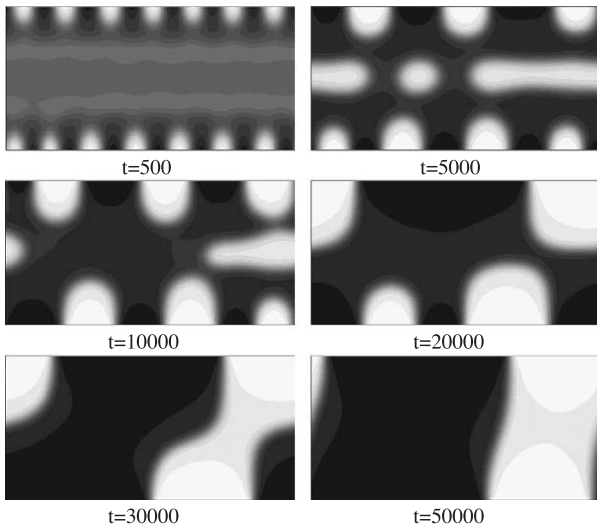


Fig. 7. The long-time microstructural evolution of a stressed, edge-supported film of composition $c_o=0.4$ is depicted with $L_2=45$, $\eta=0.02$, and $s_1=0$. As in Fig. 4b, regularly spaced, alternating regions of A -rich (black) and B -rich (white) phases form at the free surfaces. However, the B -rich surface particles remain spatially isolated and do not continue to grow vertically into the interior. Considerable coarsening of the B -rich surface particles occurs, until those at the top and bottom link-up. Subsequently, a single vertical strip of B -rich phase emerges at very long times.

that reduces the number of layers, but respects the vertical alignment of phases. The evolutions depicted in Figs. 4 and 5 depend not only on the magnitude of the compositional strain, but also on the initial composition, and on the imposed mechanical boundary conditions.

In general, there is a competition between the chemical driving force, the surface interaction, and the elastic energy in determining the kinetics of the phase decomposition. This interaction is illustrated in Fig. 6, where the effects of elasticity and surface energy interaction are combined. The two films in Fig. 6 are the same as those appearing in Figs. 4b and 5a; ($L_2=45$, $c_o=0.5$, $\eta=0.02$), except that the surface interaction is now set to $s_1=0.001$ in Fig. 6a, and to $s_1=0.01$ in Fig. 6b. In both cases, the surface energy is lowered by the segregation of A atoms to the surface.

In Fig. 6a, a thin A -rich (dark grey) layer forms in the early stages of decomposition at each surface due to the surface interaction term ($t=100$), and a faint horizontal alignment of the microstructure begins to develop ($t=100$ and 180). The compositional strain soon destabilizes the homogeneous surface layers, and a vertical realignment of the microstructure begins at the surfaces ($t=180$ and 260). Lamellar structures grow perpendicularly from the top and bottom surfaces ($t=340$) but are met in the middle of the film by two horizontally aligned layers ($t=500$), remnants of the early surface interaction effect. In Fig. 6b, the surface interaction dominates the early stage kinetics, and the entire microstructure becomes horizontally aligned ($t=260$ and 340). This arrangement exists at high cost to the elastic energy, which is reduced by a microstructure with a vertical alignment of the phases. Much later, by about $t=2000$, the

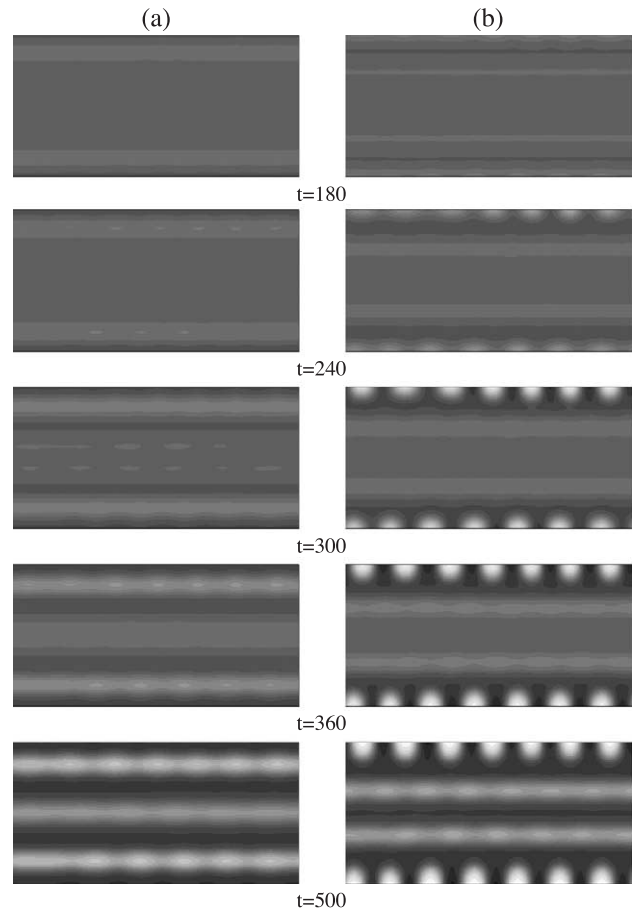


Fig. 8. The initial stages of microstructural evolution of two stressed, edge-supported films of composition $c_o=0.4$ are depicted for $L_2=45$ and $\eta=0.02$. In (a) ($s_1=0.01$), A -rich phase (dark grey) segregates to the surface, while in (b) ($s_1=-0.01$), B -rich phase (light grey) segregates to the surface due to the surface interactions. In (b), the B -rich layer quickly destabilizes forming alternating A - and B -rich phases perpendicular to the surface. In (a), the surface layer eventually becomes morphologically unstable at longer times.

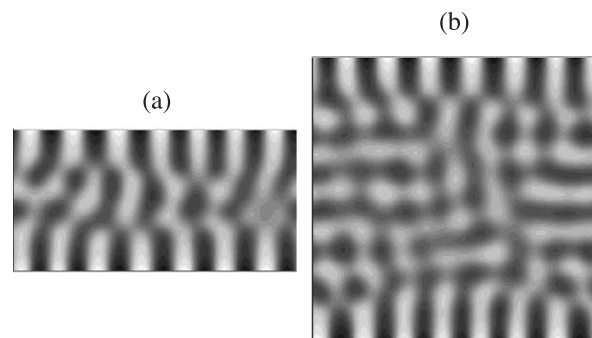


Fig. 9. The microstructure of two stressed, edge-supported films with thicknesses (a) $L_2=45$, and (b) $L_2=90$ are compared at time $t=500$ for $\eta=0.02$, $s_1=0$, and $c_o=0.5$. In both films random fluctuations in the interior of the film grow and prevent the coherent link-up of the surface lamella. Coherency quickly establishes in the thinner film (a), as is seen in Fig. 5a. In the thicker film (b) this is not the case; the phases will become aligned in both elastically soft directions, before aligning vertically at a much later time.

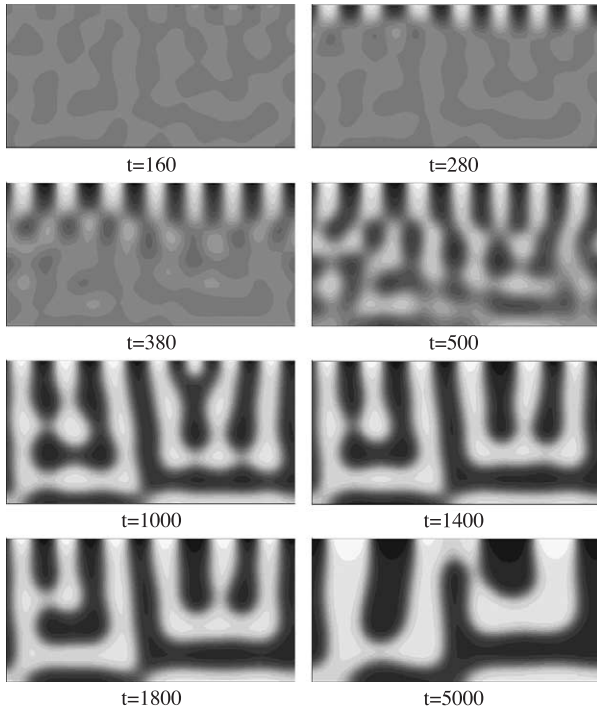


Fig. 10. The microstructural evolution of a stressed, bottom-supported film of composition $c_f=0.5$ is depicted to $t=5000$. ($L_2=45$, $\eta=0.02$, and $s_1=0$). As in the edge-supported films, vertically aligned lamella grow from the unconstrained (top) surface. Near the bottom clamped boundary, however, the phases align parallel to the surface and, eventually, a comb-like structure emerges at longer times.

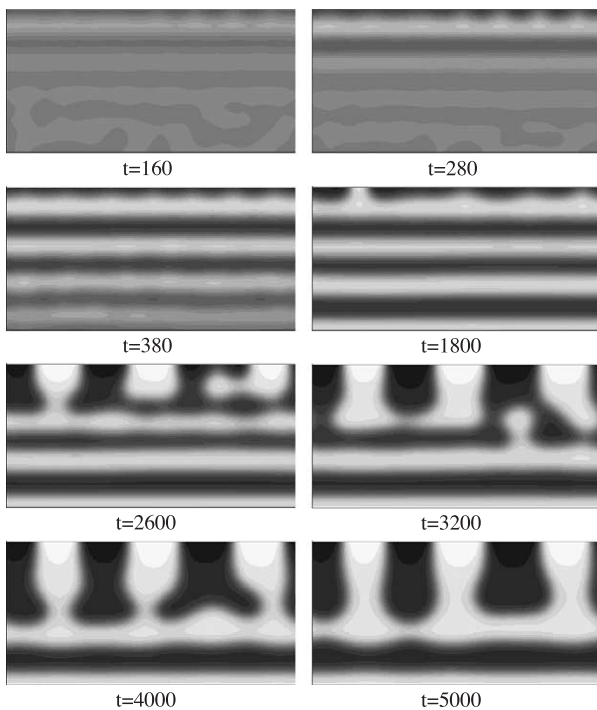


Fig. 11. The microstructural evolution of a stressed, bottom-supported film of composition $c_f=0.5$ is depicted to $t=5000$ for $L_2=45$, $\eta=0.02$, and $s_1=0.01$. Due to the surface interaction, A -rich (black) phase segregates to the free surface (top), and a horizontal alignment of the phases develops. Later ($t>1800$), the elasticity begins to realign the phases vertically near the top, unconstrained surface.

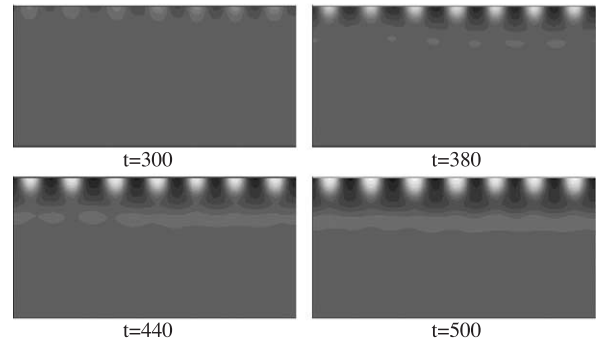


Fig. 12. The initial stages of phase decomposition for a stressed, bottom-supported film of composition $c_f=0.4$ is depicted. ($L_2=45$, $\eta=0.02$, and $s_1=0$). Due to elasticity, regularly spaced, alternating regions of A -rich (black) and B -rich (white) phases form at the surface (top). As in Fig. 7, the B -rich regions become isolated from each other and do not initially grow into the interior.

elasticity succeeds at destabilizing the surface layers, and some vertical alignment near the surface follows. This effect can be seen in Fig. 11.

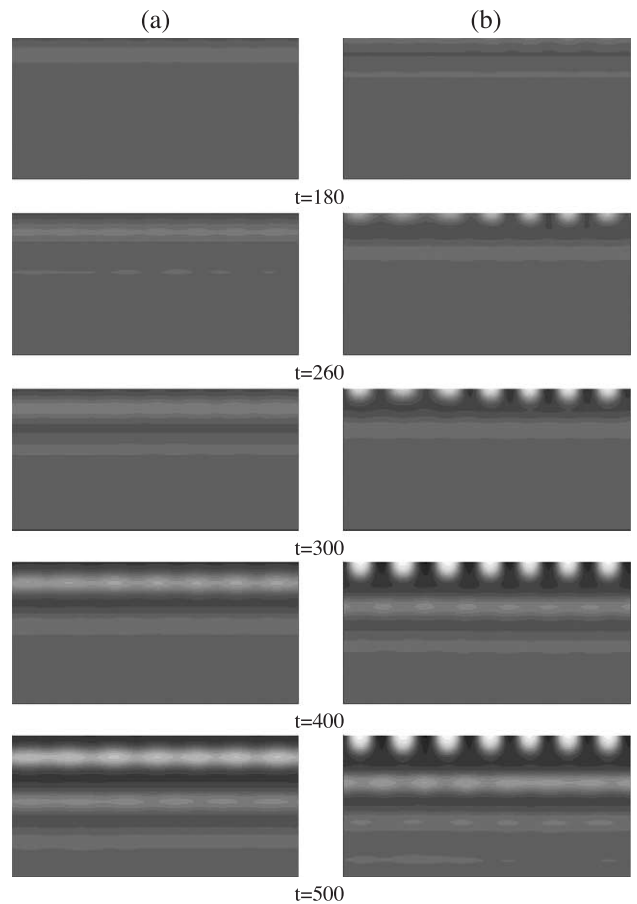


Fig. 13. The early stages of phase decomposition for two stressed, bottom-supported films of composition $c_f=0.4$ are depicted for $L_2=45$ and $\eta=0.02$. The surface energy parameters are (a) $s_1=0.01$ and (b) $s_1=-0.01$. In (a), an A -rich (black) layer forms on the top free surface while in (b), a B -rich (light gray) layer forms at the free surface. As in Fig. 8b, the B -rich layer quickly destabilizes forming alternating A - and B -rich phases perpendicular to the surface. The surface interaction prevents any vertical alignment before $t=500$ in (a).

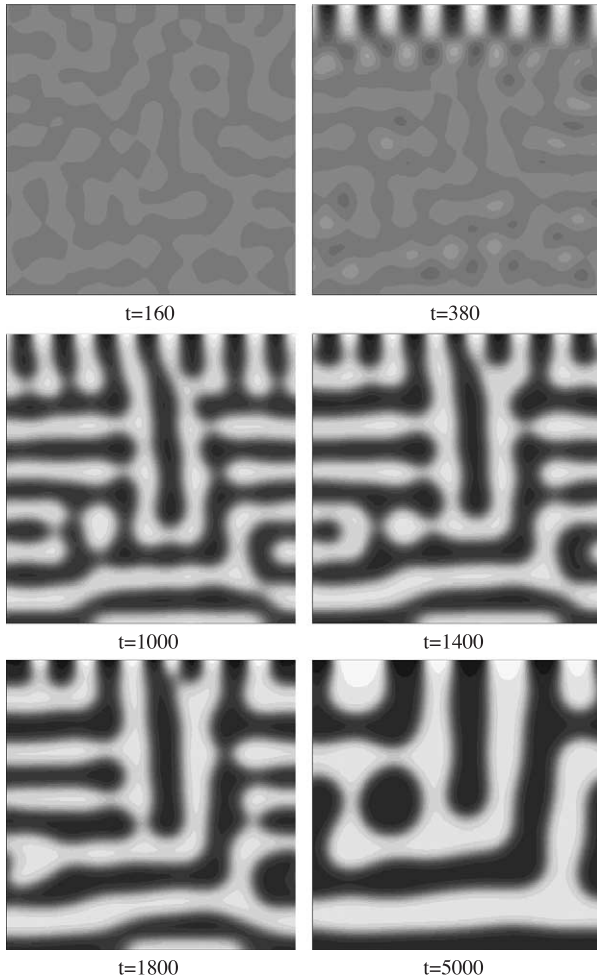


Fig. 14. The microstructural evolution of a stressed, bottom-supported film of composition $c_f=0.5$ is depicted for $L_2=90$, $\eta=0.02$, and $s_1=0$. As in Fig. 10, lamella grow perpendicular from the surface (top). Random fluctuations in the film center have time to grow, forming a microstructure with phases oriented in both elastically soft directions. In the later stages of decomposition, a vertical alignment emerges in the top half of the film.

Fig. 6 illustrates the competition between the surface interaction, which tends to produce an alignment of phases parallel with the surface, and the compositional strain, which, under certain specific conditions, tends to produce an alignment perpendicular to the surface. This has interesting implications for the theory of wetting transitions in solid materials. In his work on wetting, Cahn [9] considered critical fluid mixtures with the surface interaction energy used here. The results from Fig. 6 suggest that the elastic effect should also be included in solid mixtures in order to characterize correctly phase equilibria near a surface.

The long-time microstructural evolution of a stressed, edge-supported film of composition $c_o=0.4$ is depicted in Fig. 7. Except for the average composition, the other parameters are the same as those used for the films depicted in Figs. 4b and 5a: $L_2=45$, $\eta=0.02$, and $s_1=0$. As in Fig. 4b, regularly spaced, alternating vertical regions of *A*-rich (black) and *B*-rich (white) phases form on the surface, due to the effect of elasticity. However, unlike in Fig. 4b, the *B*-

rich (white) particles become isolated and do not continue to grow vertically into the interior ($t=5000$). Considerable coarsening of the *B*-rich surface particles occurs, until those at the top and bottom link-up. Subsequently, a single vertical strip of *B*-rich phase emerges. For the simple model of misfit used here (Vegard's law), such an arrangement produces no net misfit (as for $c_o=0.5$), and therefore requires no net displacement in the horizontal direction. Though the elastic driving force achieves vertical alignment of phases in both the edge-supported films of Fig. 5a ($c_o=0.5$) and Fig. 7 ($c_o=0.4$) at long times, the routes taken are quite different.

For off-critical mixtures, the sign of the surface energy parameter is important because the equilibrium compositions are no longer symmetric about the average composition. Fig. 8 depicts the evolution of two stressed, edge-supported films of composition $c_o=0.4$. The films are the same as those depicted in Fig. 7, except that there is now a surface interaction energy. The simulation parameters used are $L_2=45$ and $\eta=0.02$, with $s_1=0.01$ in Fig. 8a and $s_1=-0.01$ in Fig. 8b.

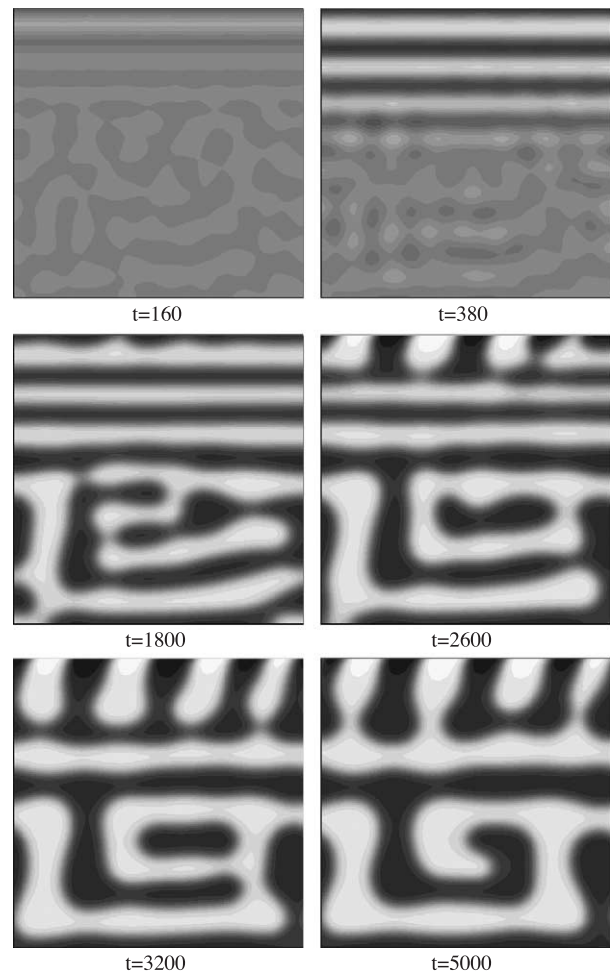


Fig. 15. The microstructural evolution of a stressed, bottom-supported film of composition $c_f=0.5$ is depicted for $L_2=90$, $\eta=0.02$, and $s_1=0.01$. Initially phase alignment is parallel to the free surface; but this microstructure is eventually destabilized owing to compositional strain effects.

The surface energy is lowered by the presence of the A -rich phase at the surface in Fig. 8a ($s_1 > 0$). In the initial stages of decomposition, A atoms segregate to the free surfaces, forming thin A -rich (dark grey) surface layers. Subsequently, the microstructure becomes horizontally aligned. The compositional strain attempts to destabilize the horizontal layers nearest to the surface in order to form a vertical alignment of phases, though by $t=500$ this has not been accomplished. Since the surface interaction parameter is negative in Fig. 8b, a B -rich (light gray) layer forms initially at the surface. This B -rich layer quickly becomes unstable, due to elasticity, and alternating A -rich (black) and B -rich (white) phase regions establish at the surface. As in Fig. 7, the B -rich regions are spatially isolated, and do not grow into the interior. At $t=500$ the horizontal layers in the center of the film are remnants of the early effect of the surface interaction energy. Fig. 8 demonstrates that, for off-critical mixtures, the sign of the surface energy parameter is important for determining the interaction between the surface and elastic effect and, therefore, the kinetics of decomposition and the microstructure that forms.

Fig. 9 shows the influence of film thickness on the elastically induced phase alignment. The microstructures of two stressed films of composition $c_o=0.5$ are displayed at non-dimensional time $t=500$. The thickness of the film in Fig. 9a is $L_2=45$, and that of the film in Fig. 9b is $L_2=90$. The compositional strain is $\eta=0.02$ and there is no surface interaction ($s_1=0$). The film in Fig. 9a is taken from Fig. 4b at non-dimensional time $t=500$.

In both films random fluctuations in the interior of the film grow and prevent the coherent link-up of the surface lamella. Coherency quickly establishes in the thinner film (a), as is seen in Fig. 5a. In the thicker film (b) this is not the case. Initially, the phases become aligned in both elastically soft directions, except near the surface where the alignment is vertical. However, at a much later time ($t \approx 7500$, not shown), a regular, vertical alignment of phases attains. Thus, one effect of increasing the film thickness is to delay, not necessarily prevent, the elastically preferred alignment of phases by introducing more randomness into phase decomposition.

3.2.2. Bottom-supported thin films

This section is concerned with spinodal decomposition in bottom-supported thin films (Fig. 1b). While the boundary conditions for the bottom-supported film are different from those for the edge-supported film (2.3), there are some similarities between the systems. First, there is a free surface in the boundary-supported film. This, as has been seen, is a preferential site for the growth of composition fluctuations from an elastic energy point of view. Second, the periodic boundary conditions at the left and right side edges of the bottom-supported film provide the same constraint on deformation as that in the edge-supported film. Namely, no net horizontal expansion or contraction can occur. Thus the elasticity effects seen at the free surfaces in the edge-

supported films should translate, to some extent, to the single free surface of the bottom-supported films.

In Fig. 10, the long-time microstructural evolution of a stressed, bottom-supported film of composition $c_o=0.5$ is depicted. The non-dimensional thickness of the film is $L_2=45$; the compositional strain is $\eta=0.02$; and there is no surface interaction ($s_1=0$). As in the edge-supported film (Figs. 4b and 5), surface-directed decomposition occurs, and a lamellar structure grows vertically from the free surface into the interior of the film. However, in marked contrast from the edge-supported systems, the film decomposes last at the bottom surface, where the film is clamped and phase separation requires the most elastic energy. Near the bottom, the microstructure becomes aligned in the horizontal direction, and by $t=5000$ a comb-like structure emerges.

Fig. 11 shows the effect of a surface interaction in bottom-supported thin films. The film in Fig. 11 has composition $c_o=0.5$; the non-dimensional thickness is $L_2=45$; the compositional strain is $\eta=0.02$; and the surface energy parameter is $s_1=0.01$. The early-time evolution seen in Fig. 11 compares well with that seen in Fig. 6b for an edge-supported film. Due to the surface interaction, an A -rich (black) layer forms at the free surface (top), and a horizontal alignment emerges. By $t=1800$ the compositional strains destabilize the surface layers and begin to realign the microstructure vertically. By $t=5000$ a structure similar to that seen in Fig. 10 emerges.

If the surface interaction parameter, s_1 , is large, the compositional strains may not be strong enough to destabilize the surface layers at all. For the case that $s_1=0.1$ with all other parameters as in Fig. 6b (edge-supported) or Fig. 11 (bottom-supported), which is not shown, the surface layers are not destabilized and the phases remain aligned parallel to the free surface up to $t=5000$.

As for the edge-supported films, moving to an off-critical composition dramatically changes the effects due to compositional strains. In Figs. 12 and 13, the microstructural evolutions of three stressed, bottom-supported films of composition $c_o=0.4$ are depicted. The non-dimensional thickness of the films is $L_2=45$; and the compositional strain is $\eta=0.02$. In Fig. 12 there is no surface interaction ($s_1=0$); in Fig. 13a, the surface energy parameter is $s_1=0.01$; and in Fig. 13b the surface parameter is $s_1=-0.01$.

The evolutions seen in Figs. 12 and 13 are similar to those depicted in Figs. 7 and 8. With no surface interaction (Fig. 12), alternating A -rich (black) and B -rich (white) phase regions form on the free surface. The B -rich regions become isolated from one another and do not grow into the interior of the film. When $s_1=0.01$ (Fig. 13a), an A -rich (dark grey) layer forms on the free surface in the initial stages of decomposition, and a horizontal alignment of the microstructure establishes. The elastic energy works to destabilize the surface layers. However, by $t=500$ it is not able to accomplish this. When $s_1=-0.01$ (Fig. 13b), a B -rich (light gray) layer forms on the free surface in the initial stages of decomposition. Due to elasticity, the layer quickly desta-

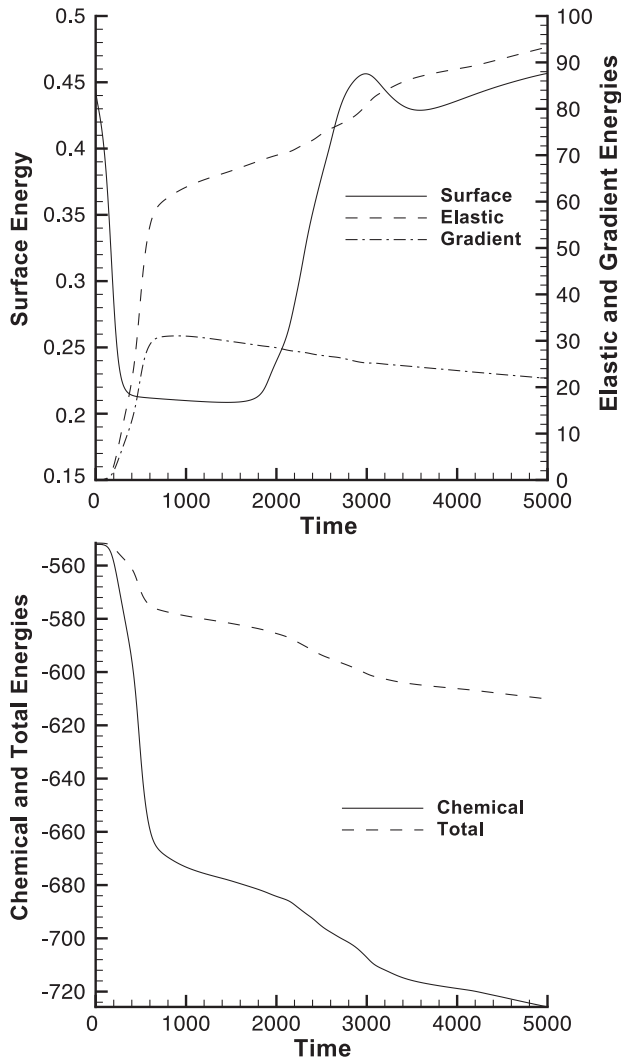


Fig. 16. Plots of the surface, elastic, gradient, chemical, and total energies, as functions of (dimensionless) time, for the simulation shown in Fig. 15. Notice that the surface energy initially decreases, and has a local minimum at about $t=1500$. Subsequently, the surface energy increases as the elasticity begins to destabilize the parallel alignment of phases.

bilizes, forming alternating *A*-rich (black) and *B*-rich (white) regions on the surface; the *B*-rich regions become isolated shortly thereafter.

The long-time microstructural evolutions depicted in Figs. 14 and 15 show the effect of film thickness on spinodal decomposition in the bottom-supported films. The systems in Figs. 14 and 15 have the following parameters: $c_0=0.5$, $L_2=90$, and $\eta=0.02$. There is no surface interaction in Fig. 14 ($s_1=0$), but in Fig. 15 $s_1=0.01$.

In Fig. 14, lamellar structures grow from the free surface into the interior of the film due to the compositional strains, as in Fig. 10, where $L_2=45$. However, there is sufficient time for random fluctuations to grow in the interior of the film, and a structure with orientations along both elastically soft directions emerges. This prohibits the lamella from growing completely through the film. Near the bottom clamped boundary, the microstructure is becoming more

horizontally aligned with increasing time, while near the traction-free surface, the phases are aligning perpendicular to the surface.

In Fig. 15, *A* atoms segregate initially to the free surface, due to the surface interaction, and the surface region becomes horizontally aligned. In the bottom half of the film, random fluctuations in the composition have sufficient time to grow, as in Fig. 14. The compositional strains then begin to realign the region near the free surface vertically. The elasticity accomplishes this by destabilizing one horizontal layer at a time, moving from the free surface into the interior. At $t=5000$ a comb-like structure emerges in the top half of the film; in the bottom half a complex microstructure is evolving.

In Fig. 16 we show the surface, elastic, gradient, chemical, and total energies, as functions of (dimensionless) time, for the simulation shown in Fig. 15. Note that the difference between the maximum and minimum values of the surface energy is much smaller than those of the elastic, gradient, and chemical energies. This is expected since it arises only from a surface density, and the others from bulk densities. Yet, the surface energy has a big impact on the microstructural evolution, as can be seen comparing Figs. 14 and 15. The behavior of the chemical and interfacial energies is typical of spinodal decomposition. The gradient energy experiences a sharp increase (phase separation), and after some time begins to slowly decrease as interfaces are eliminated during coarsening. The chemical energy is monotone in time, experiencing a rapid decrease (phase separation), then a more gradual decrease (coarsening).

Initially, the surface energy rapidly decreases, as the *A*-rich wetting layer establishes. At the same time, the elastic energy is rapidly increasing in response to the developing misfit at the surface and in the bulk. From between about $t=500$ to $t=1500$ the decrease in surface energy slows; and the surface energy has a minimum at $t \approx 1500$. After the elasticity begins to destabilize the parallel alignment, the surface energy begins to rapidly rise. One can see from Fig. 15 that the first appearance of destabilization occurs at $t \approx 1800$, coinciding with the increase in surface energy. By $t=3000$ the surface energy returns to approximately the level at $t=0$. This is expected, since the average composition at the interface is nearly 0.5.

4. Summary

In this paper we developed a diffuse interface model to study the combined effects of the surface interaction, compositional strain, and mechanical boundary conditions on surface-directed spinodal decomposition in stressed, binary thin films. Specifically, we used two-dimensional simulations to demonstrate that the kinetics of spinodal decomposition and the resulting microstructure can depend strongly on the magnitude of compositional strain,

the average film composition, the sign and magnitude of the surface interaction parameter, and the thickness of the film.

When the surface interaction term is negligible ($s_1 \approx 0$) and the compositional strain is small, composition fluctuations tend to grow uniformly throughout the film. For larger compositional strains, the composition fluctuations grow preferentially at the surface owing to the accompanying decrease in the elastic energy and, consequently, a greater net driving force for phase separation. The phases tend to align themselves perpendicular to the free surface for both the edge-supported and bottom-supported films.

A competition between the surface interaction, which tends to produce an alignment of phases parallel to the surface, and the elastic energy, which tends to produce an alignment of phases perpendicular to the surface, is observed in films where both effects are present. In certain cases, the near-surface microstructure was aligned parallel to the surface, due to the surface interaction, but then later realigned perpendicular to the surface, due to the elastic effect. This rearrangement of the microstructure lowers the elastic energy of the film. If the magnitude of the surface energy parameter is large enough, no elastic realignment is observed during the simulation. For films of off-critical composition, the sign of the surface energy parameter was seen to be important. For films of composition $c_0=0.4$, if A atoms initially segregated to the free surface, vertical phase realignment came significantly later than if B atoms initially segregated to the free surface.

For critical-composition films of large enough thickness, random fluctuations in the interior of the film had sufficient time to grow, and could prevent the uniform growth of the lamella from the surface through the film. If the film was small enough such randomness was not present, and the alignment of the phases was significantly more uniform.

Acknowledgements

This work was supported primarily through the MRSEC Center for Nanoscopic Materials Design by the National Science Foundation under Award Number DMR-0080016. In addition, JSK acknowledges the support of NSF-DMS-0314387. We acknowledge the Mathematics Department and the Networking and Academic Computing Services, both at UC Irvine, for computing time and assistance. SMW and JSK thank Prof. John Lowengrub and Prof. Vittorio Cristini for helpful discussions.

Appendix A. Nonlinear multigrid method

In this appendix, we briefly describe an efficient, fully second-order accurate, nonlinear multigrid method for the

CH and elasticity equations. This is an extension of the method for CH fluids developed [19]. As multigrid is essentially a method for accelerating convergence of a local error relaxer (smoother), e.g., Gauss–Seidel, to condense the discussion we describe only the relaxation step of the method. We assume a basic knowledge of linear multigrid methods, and the Full Approximation Storage multigrid method for nonlinear elliptic equations [20]. We note that our method is easily extended to three dimensions.

Let N_1 and N_2 be positive, even integers, and define the spatial step sizes $h_1=L_1/N_1$ and $h_2=L_2/N_2$. For simplicity we take $h=h_1=h_2$. Consider a regular $N_1 \times N_2$ grid over the computational domain D . The concentration and chemical potential are sampled at the cell centers of the grid, $((i-0.5)h, (j-0.5)h)$, where $1 \leq i \leq N_1$ and $1 \leq j \leq N_2$, and the approximations are denoted $c_{i,j}$ and $\mu_{i,j}$, respectively.

We define the discrete differentiation operators

$$D_1 c_{i+\frac{1}{2},j} = \frac{c_{i+1,j} - c_{i,j}}{h}, \quad D_2 c_{i,j+\frac{1}{2}} = \frac{c_{i,j+1} - c_{i,j}}{h}$$

which are defined on the west and north cell edges, and with these discretize the gradient operator by

$$\nabla_d \cdot c_{i,j} = \left(D_1 c_{i+\frac{1}{2},j}, D_2 c_{i,j+\frac{1}{2}} \right)$$

Correspondingly, the divergence is defined at the cell centers using samples from the cell edges:

$$\nabla_d \vec{g}_{i,j} = \frac{g_{i+\frac{1}{2},j}^1 - g_{i-\frac{1}{2},j}^1}{h} + \frac{g_{i,j+\frac{1}{2}}^2 - g_{i,j-\frac{1}{2}}^2}{h}$$

where $\vec{g}_{i,j} = (g_{i+\frac{1}{2},j}^1, g_{i,j+\frac{1}{2}}^2)$. The discretized Laplacian is defined as $\nabla_d^2 c_{i,j} = \nabla_d \cdot (\nabla_d c_{i,j})$.

We discretize the CH Eq. (11) in time using a Crank–Nicholson scheme:

$$\frac{c_{i,j}^{n+1} - c_{i,j}^n}{\Delta t} = \nabla_d \cdot \left[M(c)_{i,j}^{n+\frac{1}{2}} \nabla_d \mu_{i,j}^{n+\frac{1}{2}} \right], \quad (\text{A.1})$$

$$\begin{aligned} \mu_{i,j}^{n+\frac{1}{2}} &= \frac{1}{2} \left(\frac{df_{\text{ch}}}{dc} (c_{i,j}^{n+1}) + \frac{df_{\text{ch}}}{dc} (c_{i,j}^n) \right) + \frac{\partial f_{\text{el}}}{\partial c} (c_{i,j}^{n+\frac{1}{2}}) \\ &\quad - \frac{1}{2} \Delta d^2 (c_{i,j}^{n+1} + c_{i,j}^n), \end{aligned} \quad (\text{A.2})$$

where $M(c)=c(1-c)$ is the mobility, which must be interpolated to the cell edges. We take as source terms

$$\begin{aligned} s_{i,j}^{(1)} &= \frac{c_{i,j}}{\Delta t} \\ s_{i,j}^{(2)} &= \frac{1}{2} \left(\frac{df_{\text{ch}}}{dc} (c_{i,j}^n) - \Delta d^2 c_{i,j}^n \right) + \frac{\partial f_{\text{el}}}{\partial c} (c_{i,j}^{n+\frac{1}{2}}) \end{aligned}$$

which are known at time step n . Indeed, to get $\partial f_{\text{el}} / \partial c (c^{n+1/2})$ we (i) extrapolate the concentration from times $n-1$ and n , obtaining an approximation of $c^{n+1/2}$, and then (ii) solve the elasticity Eqs. (12) and (13) using a linear multigrid method.

Rewriting Eq. (A.1), we have

$$\begin{aligned} \frac{c_{ij}^{n+1}}{\Delta t} + \left(\frac{M(c)_{i+\frac{1}{2},j}^{n+\frac{1}{2}} + M(c)_{i-\frac{1}{2},j}^{n+\frac{1}{2}} + M(c)_{i,j+\frac{1}{2}}^{n+\frac{1}{2}} + M(c)_{i,j-\frac{1}{2}}^{n+\frac{1}{2}}}{h^2} \right) \mu_{ij}^{n+\frac{1}{2}} = s_{ij}^{(1)} \\ + \frac{M(c)_{i+\frac{1}{2},j}^{n+\frac{1}{2}} \mu_{i+1,j}^{n+\frac{1}{2}} + M(c)_{i-\frac{1}{2},j}^{n+\frac{1}{2}} \mu_{i-1,j}^{n+\frac{1}{2}} + M(c)_{i,j+\frac{1}{2}}^{n+\frac{1}{2}} \mu_{i,j+1}^{n+\frac{1}{2}} + M(c)_{i,j-\frac{1}{2}}^{n+\frac{1}{2}} \mu_{i,j-1}^{n+\frac{1}{2}}}{h^2} \end{aligned} \quad (\text{A.3})$$

Since $\text{d}f_{\text{ch}}/\text{d}c(c_{ij}^{n+1})$ is nonlinear with respect to c_{ij}^{n+1} , we linearize at c_{ij}^m , i.e.,

$$\frac{\text{d}f_{\text{ch}}}{\text{d}c}(c_{ij}^{n+1}) \approx \frac{\text{d}f_{\text{ch}}}{\text{d}c}(c_{ij}^m) + \frac{\text{d}^2 f_{\text{ch}}(c_{ij}^m)}{\text{d}c^2}(c_{ij}^{n+1} - c_{ij}^m) \quad (\text{A.4})$$

After substitution of Eq. (A.4) into Eq. (A.2), we get

$$\begin{aligned} - \left(\frac{2}{h^2} + \frac{1}{2} \frac{\text{d}^2 f_{\text{ch}}}{\text{d}c^2}(c_{ij}^m) \right) c_{ij}^{n+1} + \mu_{ij}^{n+\frac{1}{2}} \\ = s_{ij}^{(2)} + \frac{1}{2} \frac{\text{d}f_{\text{ch}}}{\text{d}c}(c_{ij}^m) - \frac{1}{2} \frac{\text{d}^2 f_{\text{ch}}(c_{ij}^m)}{\text{d}c^2} c_{ij}^m \\ - \frac{1}{2h^2} (c_{i+1,j}^{n+1} + c_{i-1,j}^{n+1} + c_{i,j+1}^{n+1} + c_{i,j-1}^{n+1}). \end{aligned} \quad (\text{A.5})$$

Finally, to obtain a Gauss–Seidel-type relaxation scheme, we use a local linearization scheme. Namely, we replace $c_{k,l}^{n+1}$ and $\mu_{k,l}^{n+1/2}$ in Eqs. (A.3) and (A.5) with $\bar{c}_{k,l}^m$ and $\bar{\mu}_{k,l}^{m-1/2}$ if $k \leq i$ and $l \leq j$, otherwise with $c_{k,l}^m$ and $\mu_{k,l}^{m-1/2}$, where an overbar denotes the latest iterate, and m is the iteration number. Thus

$$\begin{aligned} \frac{\bar{c}_{ij}^m}{\Delta t} + \left(\frac{M(c)_{i+\frac{1}{2},j}^{m-\frac{1}{2}} + M(c)_{i-\frac{1}{2},j}^{m-\frac{1}{2}} + M(c)_{i,j+\frac{1}{2}}^{m-\frac{1}{2}} + M(c)_{i,j-\frac{1}{2}}^{m-\frac{1}{2}}}{h^2} \right) \bar{\mu}_{ij}^{m-\frac{1}{2}} = s_{ij}^{(1)} \\ + \frac{M(c)_{i+\frac{1}{2},j}^{m-\frac{1}{2}} \bar{\mu}_{i+1,j}^{m-\frac{1}{2}} + M(c)_{i-\frac{1}{2},j}^{m-\frac{1}{2}} \bar{\mu}_{i-1,j}^{m-\frac{1}{2}} + M(c)_{i,j+\frac{1}{2}}^{m-\frac{1}{2}} \bar{\mu}_{i,j+1}^{m-\frac{1}{2}} + M(c)_{i,j-\frac{1}{2}}^{m-\frac{1}{2}} \bar{\mu}_{i,j-1}^{m-\frac{1}{2}}}{h^2}, \end{aligned} \quad (\text{A.6})$$

where $M(c)_{i+1/2,j}^{m-1/2} = M((c_{ij}^m + c_{i+1,j}^m + c_{i,j}^n + c_{i+1,j}^n)/4)$ (the other terms are similarly defined), and

$$\begin{aligned} - \left(\frac{2}{h^2} + \frac{1}{2} \frac{\text{d}^2 f_{\text{ch}}}{\text{d}c^2}(c_{ij}^m) \right) \bar{c}_{ij}^m + \bar{\mu}_{ij}^{m-\frac{1}{2}} \\ = s_{ij}^{(2)} + \frac{1}{2} \frac{\text{d}f_{\text{ch}}}{\text{d}c}(c_{ij}^m) - \frac{1}{2} \frac{\text{d}^2 f_{\text{ch}}}{\text{d}c^2}(c_{ij}^m) c_{ij}^m \\ - \frac{1}{2h^2} (c_{i+1,j}^m + \bar{c}_{i-1,j}^m + c_{i,j+1}^m + \bar{c}_{i,j-1}^m) \end{aligned} \quad (\text{A.7})$$

We solve the two linear equations (Eqs. (A.6) and (A.7)) by 2×2 matrix inversion. To start the iteration process we set $c_{k,l}^{m=0} = c_{k,l}^n$ and $\mu_{k,l}^{m-1/2=-1/2} = \mu_{k,l}^{n-1/2}$; and after we have performed m_s smoothing iterations using Gauss–Seidel we set $c_{k,l}^{n+1} = \bar{c}_{k,l}^{m_s}$ and $\mu_{k,l}^{n+1/2} = \bar{\mu}_{k,l}^{m_s-1/2}$.

References

- [1] J.W. Cahn, J.E. Hilliard, J. Chem. Phys. 28 (1958) 258.
- [2] J.W. Cahn, Acta Metall. 9 (1961) 795.
- [3] R.C. Ball, R.H.L. Essery, J. Phys., Condens. Matter 2 (1990) 10303.
- [4] G. Brown, A. Chakrabarti, Phys. Rev. A 46 (1992) 4829.
- [5] S. Puri, K. Binder, J. Stat. Phys. 77 (1994) 145.
- [6] C. Geng, L.-Q. Chen, Surf. Sci. 355 (1996) 229.
- [7] B.P. Lee, J.F. Douglas, S.C. Glotzer, Phys. Rev., E 60 (1999) 5812.
- [8] W.C. Johnson, Acta Mater. 49 (2001) 3463.
- [9] J.W. Cahn, J. Chem. Phys. 66 (1977) 3667.
- [10] R.A.L. Jones, L.J. Norton, E.J. Kramer, F.S. Bates, P. Wiltzius, Phys. Rev. Lett. 66 (1991) 1326.
- [11] F. Bruder, R. Brenn, Phys. Rev. Lett. 69 (1992) 624.
- [12] G. Krausch, C.-A. Dai, E.J. Kramer, F.S. Bates, Phys. Rev. Lett. 71 (1993) 3669.
- [13] K.T. Moore, W.C. Johnson, J.M. Howe, H.I. Aaronson, D.R. Veblen, Acta Mater. 50 (2002) 943.
- [14] J.W. Cahn, R. Kobayashi, Acta Metall. Mater. 43 (1995) 931.
- [15] D.J. Seol, S.Y. Hu, Y.L. Li, J. Shen, K.H. Oh, L.Q. Chen, Met. Mater. Int. 9 (2003) 61.
- [16] D.J. Seol, S.Y. Hu, Y.L. Li, J. Shen, K.H. Oh, L.Q. Chen, Acta Mater. 51 (2003) 5173.
- [17] S.M. Wise, PhD thesis, University of Virginia, Charlottesville, VA, United States, 2003.
- [18] A.G. Kachaturyan, Theory of Structural Transformations in Solids, John Wiley & Sons, Berlin, 1983.
- [19] J.S. Kim, K. Kang, J.S. Lowengrub, J. Comp. Phys. 193 (2004) 511.
- [20] U. Trottenberg, C. Oosterlee, A. Schüller, Multigrid, Academic Press, New York, 2001.